Applied Ocean Research 53 (2015) 31–45

Contents lists available at ScienceDirect

Applied Ocean Research

journal homepage: www.elsevier.com/locate/apor

Near-optimal control of a wave energy device in irregular waves with deterministic-model driven incident wave prediction

Umesh A. Korde *

Department of Mechanical Engineering, South Dakota School of Mines and Technology, Rapid City, SD 57701, USA

ARTICLE INFO

Article history:
Received 17 April 2015
Received in revised form 2 July 2015
Accepted 19 July 2015

Keywords:
Wave energy conversion
Control
Relative oscillation
Time-domain
Irregular waves
Deterministic propagation
Wave profile prediction

ABSTRACT

This paper investigates wave-by-wave control of a wave energy converter using incident wave prediction based on up-wave surface elevation measurement. The goal of control is to approach the hydrodynamically optimum velocity leading to optimum power absorption. This work aims to study the gains in energy conversion from a deterministic wave propagation model that accounts for a range of group velocities in deriving the prediction. The up-wave measurement distance is assumed to be small enough to allow a deterministic propagation model, and further, both wave propagation and device response are assumed to be linear. For deep water conditions and long-crested waves, the propagation process is also described using an impulse response function (e.g. [1]). Approximate low and high frequency limits for realistic band-limited spectra are used to compute the corresponding group velocity limits. The prediction time into the future is based on the device impulse response function needed for the evaluation of the control force. The up-wave distance and the duration of measurement are then determined using the group velocity limits above.

A 2-body axisymmetric heaving device is considered, for which power capture is through the relative heave oscillation between the two co-axial bodies. The power take-off is assumed to be linear and ideal as well as capable of applying the necessary resistive and reactive load components on the relative heave oscillation. The predicted wave profile is used along with device impulse response functions to compute the actuator force components at each instant. Calculations are carried out in irregular waves generated using a number of uni-modal wave spectra over a range of energy periods and significant wave heights. Results are compared with previous studies based on the use of instantaneous up-wave wave-profile measurements, both without and with oscillation constraints imposed. Considerable improvements in power capture are observed with the present approach over the range of wave conditions studied.

1. Introduction

Wave energy conversion has received considerable attention in the literature for over four decades now [2–4]. A large number of wave energy converters studied so far have consisted of a wave-activated body and a reference, for energy conversion from the relative oscillation. Since power absorption is best close to resonance and wave climates can vary widely through a year, approaches to provide active control of device oscillations have also been pursued for many years. Early efforts to increase response bandwidth by controlling the phase of the force applied by the power take-off were reported in [5,6]. This control was accomplished by including a reactive component in the load in addition to the resistive part and independently adjusting the magnitudes of the two parts. Further investigations on small heaving point-absorber devices with short resonant periods led to the development of the ‘latching’ concept [7]. This improved power capture in longer-period waves by keeping body oscillation locked and releasing it only when the velocity peak was close to matching the exciting force peak.

The decades since the seventies have witnessed a growing realization that some type of control may be essential for cost-effective implementation of wave energy converters (e.g. [8]). Thus, latching type switching control has been investigated by many researchers to date (e.g. see [9–14], etc, to name a few). The determination of an optimal latching sequence was first addressed under an optimal control framework in [9] with the dynamic model providing the dynamic constraints. The optimum switching sequence can be determined with the help of the Pontryagin Max/Min Principle (often following an iterative approach). Although latching requires no reactive load, the co-state equations describing the time-dependence of the Lagrange multipliers need to be integrated back in time from T_f to 0 in order to determine a latching sequence over $[0, T_f]$ ($T_f > t$ where t is the current time, and T_f the time into

* Tel.: +1 605 355 3731.
E-mail address: Umesh.Korde@sdsmt.edu

0141-1187/$ – see front matter © 2015 Elsevier Ltd. All rights reserved.
http://dx.doi.org/10.1016/j.apor.2015.07.007

$\eta(\cdot\,;\cdot)$	wave surface elevation at point $(\cdot)$ and time $(\cdot)$
ω	angular frequency of wave/oscillation
$\bar{a}_t(\omega)$, $\bar{a}_b(\omega)$	added mass variations for the top and bottom bodies, respectively, inclusive of infinite-frequency parts
$\varepsilon(x_A\,;t)$	measurement error in wave elevation at $(x_A\,;t)$
$\varepsilon(x_B\,;t+t_p)$	prediction error at $(x_B\,;t+t_p)$ as a result of measurement error at $(x_A\,;t)$
$\varepsilon_l(t)$, $\varepsilon_a(t)$	errors in resistive force $F_l(t)$ and reactive force component $F_a(t)$ due to measurement error in wave elevation at $(x_A\,;t)$
A	incident wave amplitude
$a_c(\omega)$, $b_c(\omega)$	added mass and radiation damping coefficients representing the frequency-dependent radiation coupling between the top and bottom bodies
$b_t(\omega)$, $b_b(\omega)$	radiation damping variations for the top and bottom bodies, respectively
c_{dt}, c_{db}	linearized, constant viscous damping coefficients for the top and bottom bodies, respectively
D	constant damping load applied on the relative heave oscillation
d	x-separation between the up-wave profile measurement location and device centroid
F_l	force applied by a power take-off actuator between the top and bottom bodies
F_{ft}, F_{fb}	exciting forces on the top and bottom bodies, respectively
$h_e(t)$	non-causal impulse response function (with respect to incident wave profile at body centroid x_B) representing the exciting force
h_l	impulse response function defining linear, unidirectional propagation of an impulsive wave elevation through a distance d
$h_l(t)$, $h_a(t)$	impulse response functions representing the resistive and reactive parts of the 'load' force applied by the power take-off
$h_o(t)$	impulse response function leading to hydrodynamically optimum relative heave velocity
$k(\omega)$	wave number; related to angular frequency ω through the dispersion relation
k_t, k_b	stiffness constants determining the restoring forces on the top and bottom bodies, respectively
$L(\omega)$, $N(\omega)$	resistive and reactive parts of the impedance generated by the power take-off
m_t, m_b	in-air masses of the top and bottom bodies, respectively
P_w	average power absorbed under approximate near-optimal control
P_{in}	time-averaged incident wave power per unit crest-length
$R_i(\omega)$, $C_i(\omega)$	equivalent hydrodynamic damping and reactance components 'acting on' the relative oscillation between the two bodies
v_r, x_r	relative heave velocity and displacement between the top and bottom bodies
v_t, v_b	heave oscillation velocities of the top and bottom bodies, respectively
v_{gmn}	minimum group velocity as determined by the high-frequency 'cut-off' for a realistic wave spectrum
v_{gmx}	maximum group velocity as determined by the low-frequency 'cut-off' for a realistic wave spectrum
x_A	x-coordinate along the propagation direction where wave profile measurement is made
x_B	x-coordinate along the propagation direction where the device centroid is located

the future up to which a latching sequence is to be determined). The formulation leads to a 2-point boundary value problem, and for this reason, the exciting force on the body needs to be predicted $(T_f - t)$ into the future. A declutching approach was developed later mainly for devices with longer resonance periods than the prevailing energy periods [15,16]. With either latching or declutching the sudden application or release of large forces/moments can lead to transient vibrations through the entire system, which, in addition to the force/moment load magnitudes, should be considered early in the design process.

Early reactive control approaches were later generalized to multiple-mode devices, and it was also shown that maximum power capture was possible under impedance matching conditions, wherein the load impedance matrix would be the complex-conjugate of the body impedance matrix in water [17–19]. This approach involves exchange of reactive power and energy storage, but enables greater energy absorption annually as long as the power take-off mechanism is capable of applying reactive loads. Non-real time applications of this approach include 'peak-frequency tuning' where the incoming wave spectra are sampled at regular intervals (e.g. 10 min) and the load impedance is adjusted so as to approach impedance matching at the spectral peak frequency. This strategy was recently tested on the wave star device [20] and a 2–3-fold improvement in annual power production was reported.

Still greater improvements are possible if optimal impedance matching can be achieved in real time on a wave-by-wave basis. However, as is well known, wave-by-wave implementation of such control is not possible without prior knowledge or estimation of the device velocity and force some duration into the future. The underlying cause of this difficulty is that the radiation force felt by an oscillating body (due to the waves it creates with its own oscillation) is causal. Thus, for the impulse response function h_r describing this force, for $t < 0$, $h_r(t) = 0$. Causality of h_r implies that the Fourier transform of h_r is an analytic function in the top half plane, so that the real and imaginary parts of its Fourier transform are constrained together by the Kramers–Kronig relations [21,22]. For impedance matching, the real part needs to be matched, and the imaginary part needs to be canceled. Because $h_r(t)$ is also real-valued, $h_r = h_a + h_b$, where h_a is an odd function, and h_b is an even function. Moreover, the two add together to zero for $t < 0$ and to h_r for $t \geq 0$. To implement impedance matching wave-by-wave, however, as mentioned, $-h_a$ and h_b need to be synthesized and utilized independently. Since both are non-causal, i.e. $h_a, h_b \neq 0$, $t < 0$, velocity information from the future is required in the generation of the control force at any instant t. This situation is discussed in [23,1]. In addition, wave action on the free surface is a continuum process over a distributed medium, and further, the body has a finite geometric size. Therefore, the body begins to experience the exciting force before the wave reaches it and before there is a wave elevation detected at its centroid. Thus, the impulse response function describing the exciting force with respect to the surface elevation at the body centroid is non-causal [1].

Hence, application of a control strategy seeking wave-by-wave impedance match requires the knowledge of the incident wave profile (and based on it, the device oscillation) in advance. In practice, future information over 25–30 s may be sufficient for a reasonable approximation to the required control force. Thus, approximate approaches based on time-series analysis were applied in [24,25]. More systematic forecasting techniques have developed in recent years [26]. A number of other control approaches seeking realistic solutions have also been investigated during the past decade [27–29]. A purely causal strategy based within a Linear Quadratic Gaussian formulation was discussed in [30]. A comparative evaluation of several control strategies was presented in [31]. Direct use of wave profile measurements some distance up-wave for evaluating the control force at the current time was considered in [32].

The need for future information to determine the present input makes Model Predictive Control (MPC) a good choice for wave energy device control, because MPC can incorporate both prediction and use, of the exciting force time-series over a prediction horizon. The goal is to determine the current control force so as optimize a cost function (e.g. the absorbed power) over the prediction horizon. The device dynamic model and any other prescribed oscillation limits then provide the 'constraints' for the optimization of the cost function. Significant gains in power capture have been reported to date (e.g. [27,33,34], etc.). MPC brings a strong control engineering formalism to bear on the problem of controlling a wave energy device, using state-space approximations for convolutions and results from matrix algebra as necessary. Predictions can be based on time-series analysis [35], on Kalman-filtering [27], or on a deterministic wave-propagation model [34].

The present approach is more directly based on the linear hydrodynamic theories and time-domain studies of the 70s and 80s respectively (e.g. see [36]). As discussed further in the following paragraphs, this work uses deterministically predicted wave elevation information to evaluate the control forces that will approximately produce the hydrodynamically optimum velocity (subject to any constraints) at the present instant. It may be recalled that, within linear theory, the unconstrained hydrodynamic velocity optimum maximizes power capture through optimum interaction among the incident, diffracted and radiated wave-fields (see for instance, [1,36,37], etc.), while an constrained optimum velocity enables the closest approach to the hydrodynamic optimum within the allowed oscillation envelope (e.g. [38]).

A sub-optimal approach was described in [32], where a simplification was made (but not explicitly stated) that the wave propagation was at the shallow-water limit for group velocity. This amounted to assuming non-dispersive propagation at a single group velocity. Thus, the control forces derived based on this assumption could use an instantaneous measurement of the surface elevation at an up-wave distance related to the prediction time and the group velocity limit. However, the controller was then most effective in spectra where longer waves were predominant, i.e. in swell dominated spectra. The present work investigates the effect of a deterministic approach[1] that accounts for a range of group velocities. The group velocity range used here is derived from the frequency range observed in commonly occurring wave spectra. The propagation model derived in [1] and the associated impulse response function is used here under deep-water conditions. As discussed in [40], two approaches to wave profile prediction using up-wave measurements are possible. One, where an instantaneous measurement/snap-shot of wave profiles over an up-wave area is used, and another, where measurements over a time duration at a single up-wave point are used. The second approach is based on the propagation model of [1] and is followed in the present work. Notable in the use of up-wave measurements to obtain wave predictions is the work based on x-band radar measurements using the WaMOS system [41]. In contrast, however, the measurement hardware assumed in the present work is a wave-rider buoy placed up-wave of the device, capable of transmitting surface elevation information using telemetry. Long-crested waves are assumed as a simplification, so that a measurement system using a single non-directional buoy is adequate. Here, for the purpose of surface-elevation prediction, no explicit account is taken in the up-wave measurement, of any scattered and radiation wave fields returning from the device. However, a 2-point measurement approach such as discussed in [42] could be employed in practical measurements for incident-wave elevation separation. As mentioned, linear superposition is assumed. However, it is of interest to note that prediction in multi-directional waves and the effect of nonlinearity are discussed in [43].

As already indicated, the goal of this paper is to investigate the effect of an approach (i) that obtains wave prediction based on up-wave measurement over a duration of time and a linear deterministic wave propagation model; (ii) and uses this prediction to generate the control forces to be applied by an actuator acting on the relative heave oscillation between two co-axial axisymmetric bodies. This type of a device has been considered by several groups in analysis and practical testing (e.g. [44,45], etc.). The theory discussed in [46] is used in arriving at the control forces, following the time-domain expressions and impulse response functions described in [47]. Note that the effect of just the feedforward control forces is studied here, and no attempt is made to apply feedback to correct for unmodeled effects, measurement errors, etc. Section 2 presents the overall formulation underlying the wave prediction approach, while Section 3 discusses the device model leading up to the control forces needed for the relative heave oscillation. Section 4 summarizes the calculations carried out in this work, and Section 5 discusses the results, with the main conclusions summarized in Section 6.

2. Approach to wave prediction

It is assumed that the irregular wave field is comprised mostly of small wave slopes and can be described as a linear superposition of small-amplitude frequency components at different amplitudes and phases. Further, since current interest here is in control in long-crested waves, propagation is assumed to be uni-directional. The direction is assumed to be left to right, with the positive x axis aligned with the propagation direction. Deep-water conditions are assumed. As discussed in [1], the contribution of a frequency component to the surface elevation at locations x_A and x_B along the x axis can be expressed as

$$\begin{aligned}\eta(x_A;i\omega)&=A(i\omega)\mathrm{e}^{-ik(\omega)x_A}\\ \eta(x_B;i\omega)&=A(i\omega)\mathrm{e}^{-ik(\omega)x_B}\end{aligned}\tag{1}$$

where point A is up-wave of B, i.e. $x_A < x_B$, and

$$x_A = x_B - d \tag{2}$$

The wave number $k(\omega)$ is related to the frequency ω through the dispersion relation

$$k\tanh kh=\frac{\omega^2}{g}\tag{3}$$

which in deep water takes the form,

$$k=\frac{\omega^2}{g},\quad \text{since},\quad \tanh kh\to 1,\quad h\to\infty\tag{4}$$

Propagation of impulsive disturbances to the free surface can be described using group velocities v_g [48,49]. The group velocity in deep water is

$$v_g=\frac{d\omega}{dk}=\frac{1}{2}\left(\frac{\omega}{k}\right)=\frac{1}{2}\left(\frac{g}{\omega}\right)\tag{5}$$

Now,

$$\eta(x_A;i\omega)=A(i\omega)\mathrm{e}^{-ik(\omega)(x_B-d)}\tag{6}$$

so that,

$$\begin{aligned}\eta(x_A;i\omega)&=\mathrm{e}^{ik(\omega)d}\eta(x_B;i\omega)\\ \eta(x_B;i\omega)&=\mathrm{e}^{-ik(\omega)d}\eta(x_A;i\omega)\end{aligned}\tag{7}$$

[1] It is interesting to note that approaches based on wave group statistics [39] may be used to tune or detune device response with the help of continual spectral measurements near a device. The present work focuses on direct use of deterministic surface elevation predictions instead.

2.1. Propagation impulse response function

The treatment in [1] is followed here as summarized below. However, this topic has also been discussed in [40] as part of the case where measurements at a single up-wave point are used to obtain a prediction. The surface elevation at location x_B as a function of time can be expressed as the inverse Fourier transform of $\eta(x_B\,; i\omega)$ as

$$\eta(x_B; t) = \frac{1}{2\pi}\int_{-\infty}^{\infty} \eta(x_B; i\omega)\mathrm{e}^{i\omega t}d\omega \tag{8}$$

It should be noted that it is the wave elevation to which Fourier transformation is applied here. For the Fourier transform to exist [50], an assumption being made here is that $\eta(\cdot\,; t)\to 0$, as $t\to\pm\infty$. For realistic spectra, $\eta(\cdot\,; i\omega)\to 0$ as $\omega\to\pm\omega_{mx}$, where $\omega_{mx}\ll\infty$. The present treatment, and the control approach based on it thus apply between successive periods of low wave activity (i.e., when energy conversion is not attempted).

Substituting the second of Eq. (7) into Eq. (8),

$$\eta(x_B; t) = \frac{1}{2\pi}\int_{-\infty}^{\infty} \mathrm{e}^{-ik(\omega)d}\eta(x_A; i\omega)\mathrm{e}^{i\omega t}d\omega \tag{9}$$

Alternatively,

$$\eta(x_B; t) = \frac{1}{2\pi}\int_{-\infty}^{\infty} H_l(i\omega)\eta(x_A; i\omega)\mathrm{e}^{i\omega t}d\omega \tag{10}$$

where $H_l(i\omega) = \exp[-ik(\omega)d]$. $H_l(i\omega)$ defines the uni-directional linear propagation process that relates the wave profile at x_B to that at x_A in the frequency domain. $\eta(x_B\,; t)$ can then be expressed using Faltung's theorem as

$$\eta(x_B; t) = \int_{-\infty}^{\infty} h_l(\tau)\eta(x_A; t-\tau)d\tau \tag{11}$$

where $h_l(t)$ is the impulse response function that defines the process in the time domain, describing the surface profile created at x_B by an impulsive surface elevation at x_A. A time dependent wave profile $\eta(x_A\,; t)$ at x_A will thus result in a profile $\eta(x_B\,; t)$ according to the linear system represented by Eq. (11). $h_l(t)$ defining this propagation process can be found as,

$$h_l(t) = \frac{1}{2\pi}\int_{-\infty}^{\infty} H_l(i\omega)\mathrm{e}^{i\omega t}d\omega \tag{12}$$

$h_l(t)$ is real-valued if $H_l(-i\omega) = H_l^*(i\omega)$. This condition is satisfied if $k(\omega)$ has the same sign as ω, or $k(\omega) = |\omega|\omega/g$. This is also consistent with rightward propagation. Thus,

$$h_l(t) = \frac{1}{2\pi}\int_{-\infty}^{\infty} \mathrm{e}^{-i(|\omega|\omega/g)d}\mathrm{e}^{i\omega t}d\omega \tag{13}$$

It can be seen, via the use of Euler's formula and some algebra, that

$$h_l(t) = \frac{1}{\pi}\int_{0}^{\infty}\left[\cos\left(\frac{|\omega|\omega}{g}d\right)\cos\omega t + \sin\left(\frac{|\omega|\omega}{g}d\right)\sin\omega t\right]d\omega \tag{14}$$

which can be written as

$$h_l(t) = \frac{1}{\pi}\int_{0}^{\infty}\cos\left(\frac{\omega^2}{g}d - \omega t\right)d\omega \tag{15}$$

$h_l(t)$ is thus seen to be real-valued, confirming that a real-valued $\eta(x_B\,; t)$ results from a real-valued $\eta(x_A\,; t)$. Following [1], it is seen from Eq. (14) that the first integrand contains a cosine function of t, and is an even function, while the second integrand contains a sine function, which is an odd function of t. It can therefore be rewritten as

$$h_l(t) = h_{le}(t) + h_{lo}(t) \tag{16}$$

Use of integration tables [51] for the integral leading to h_{le} gives,

$$h_{le}(t) = \frac{1}{4}\sqrt{\frac{2g}{\pi d}}\left[\cos\left(\frac{gt^2}{4d}\right) + \sin\left(\frac{gt^2}{4d}\right)\right] \tag{17}$$

The integral leading to h_{lo} can also be determined via integration tables [51],

$$h_{lo}(t) = \frac{1}{2}\sqrt{\frac{2g}{\pi d}}\left[\cos\left(\frac{gt^2}{4d}\right)\mathrm{C}\left(t\sqrt{\frac{g}{2\pi d}}\right) + \sin\left(\frac{gt^2}{4d}\right)\mathrm{S}\left(t\sqrt{\frac{g}{2\pi d}}\right)\right] \tag{18}$$

C and S are the Fresnel integrals. As discussed in [1,23], the impulse response function $h_l(t)$ is not causal, in that it is nonzero up to some finite values of $t<0$. This is because $|h_{le}(t)| = |h_{lo}(t)|$ only as $|t|\to\infty$. This can be seen as follows: As $t\to\infty$,

$$\mathrm{C}\left(t\sqrt{\frac{g}{2\pi d}}\right)\to\frac{1}{2};\quad \mathrm{S}\left(t\sqrt{\frac{g}{2\pi d}}\right)\to\frac{1}{2} \tag{19}$$

Thus, as $|t|\to\infty$,

$$\begin{aligned} t<0:\ & h_l(t) = h_{le}(t) + h_{lo}(t) = h_{le}(t) - |h_{lo}(t)|\to 0\\ t>0:\ & h_l(t) = h_{le}(t) + h_{lo}(t) = \frac{1}{2}\sqrt{\frac{2g}{\pi d}}\left[\cos\left(\frac{gt^2}{4d}\right) + \sin\left(\frac{gt^2}{4d}\right)\right] \end{aligned} \tag{20}$$

Over finite $|t|$, $h_l(t)$ can be written as,

$$\begin{aligned} h_l(t) = {} & \frac{1}{4}\sqrt{\frac{2g}{\pi d}}\left[\cos\left(\frac{gt^2}{4d}\right) + \sin\left(\frac{gt^2}{4d}\right)\right]\\ & + \frac{1}{2}\sqrt{\frac{2g}{\pi d}}\left[\cos\left(\frac{gt^2}{4d}\right)\mathrm{C}\left(t\sqrt{\frac{g}{2\pi d}}\right)\right.\\ & \left. + \sin\left(\frac{gt^2}{4d}\right)\mathrm{S}\left(t\sqrt{\frac{g}{2\pi d}}\right)\right] \end{aligned} \tag{21}$$

where the distance d is determined as discussed in Section 2.2. $h_l(t)$ is the impulse response function that describes the wave elevation produced at x_B by an impulsive disturbance at a point x_A, where $x_B = x_A + d$. This function is non-causal, as expected, for the deep-water condition under study [1]. A causal approximation that ignores the non-zero values of h_l for $t<0$ (i.e. approximating it to zero) is used in the calculations here.

2.2. Up-wave distance and duration of measurement

It is useful to follow the treatment of [41,43], where a space–time diagram is used to understand the propagation process. As the surface elevation at any point such as x_A is (for small amplitude waves) a linear superposition of all of the components represented in a wave spectrum, it is important to consider the entire range of propagation velocities represented in this measurement. The impulse response function h_l of Section 2.1 represents the effect of an impulsive surface elevation at x_A at a point x_B, which is a distance d down-wave in the propagation direction. The

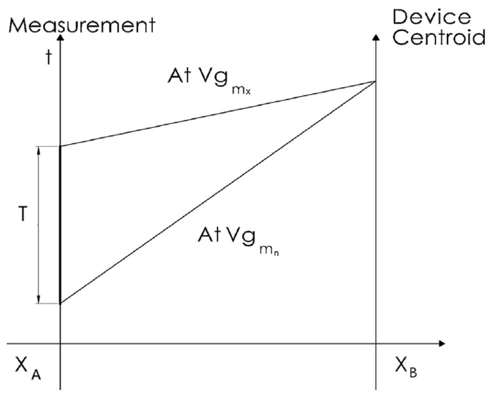

Fig. 1. Space–time diagram showing the 'influence zone' for the wave profile measurement made over $[t - T, t]$ seconds. The device location is where the measured information arrives at $t + t_P$ seconds, where t denotes the current instant, and t_P the time duration into the future at which the wave profile needs to be predicted. Note that since both device and wave sensor buoy are moored, their position coordinates are subject to precision limits depending on their respective mooring designs. This point is discussed further in Section 5.

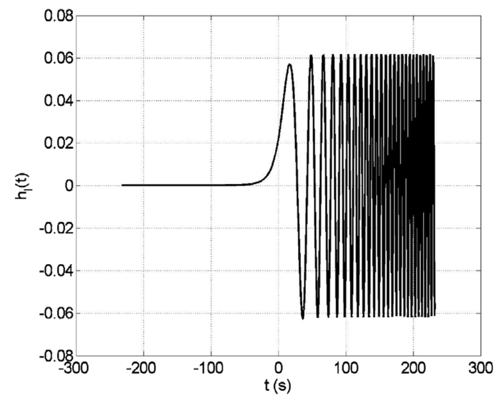

Fig. 2. Impulse response function h_l describing the propagation of a uni-directional disturbance through the distance $d = 817.5$ m. Here, $v_{gmx} = 27.22$ m/s and $v_{gmn} = 3.13$ m/s; with $t_P = 30$ s. d is computed using Eq. (25). Deep water conditions are assumed. Note that $h_l(t) \neq 0$, $t < 0$, so that h_l is non-causal. In the present calculations, h_l is set to zero for $t < 0$.

impulse causing h_l ideally represents contributions over frequencies $0 \leq \omega \leq \infty$. However, a realistic spectrum is band-limited in that wave amplitude contributions below and above certain frequencies are negligible [23]. The up-wave distance for wave measurement and the duration of measurement maybe determined by the range of group velocities represented in a prevailing spectrum where prediction is needed. The greatest frequency with nonzero contribution in the spectrum represents the slowest group velocity for wave groups in the neighborhood of this frequency. Conversely, the smallest frequency with nonzero contribution represents the fastest group velocity of waves in the neighborhood of that frequency. These two group velocity limits can be used to determine the up-wave distance and the duration of measurement needed. This point is discussed further at the end of this subsection.

Fig. 1 shows a space–time diagram with propagation distance along the x axis and time along the y axis. The point of wave measurement, namely x_A, and a suitably chosen time instant (e.g. a time prior to the instant at which measurements begin) together define the origin, and the propagation domain of interest is here the first quadrant. Any straight line starting on the positive y-axis and going out into the first quadrant represents propagation at a particular group velocity v_g. Thus, the smaller the group velocity, the longer it takes a group to propagate to the point x_B, and the steeper the slope of the line representing that v_g. By contrast, the greater the group velocity, the quicker that group covers the distance to x_B, and so the smaller its slope. Lines parallel to the x axis represent the limit $v_g \to \infty$, while the y axis represents the limit $v_g \to 0$. The maximum and minimum group velocity values associated with a realistic spectrum thus define two lines on the space–time diagram in Fig. 1. The minimum group velocity v_{gmn} results from the maximum frequency ω_{mx} represented in the spectrum (to a predetermined spectral density magnitude threshold), as

$$v_{gmn} = \frac{1}{2}\left(\frac{g}{\omega_{mx}}\right) \tag{22}$$

On the other hand, the maximum group velocity v_{gmx} can be found using the minimum frequency in the spectrum ω_{mn} (again using a predetermined spectral density magnitude threshold),

$$v_{gmx} = \frac{1}{2}\left(\frac{g}{\omega_{mn}}\right) \tag{23}$$

The region of the space-time diagram bounded by the two lines corresponding to v_{gmn} and v_{gmx} defines the region where, for the given spectrum, all of the information is available (to the approximation implied above) for a determination of the surface elevation at a chosen point from a measurement made over the time interval $[0, T]$. $(x_B, \bar{t})$ denotes the coordinate pair at the point where the two lines intersect (note that lines for other v_g, $v_{gmn} \leq v_g \leq v_{gmx}$ also intersect that this point). It represents the location in space and the point in time at which full prediction of the wave profile can be obtained using a measurement over $[0, T]$ at an up-wave location x_A. If the instant T defines the present time, then $\bar{t}$ for the point of intersection is a time in the future given by

$$\bar{t} - T = \frac{x_B - x_A}{v_{gmx}} \tag{24}$$

Defining $\bar{t} - T \equiv t_P$, the 'prediction time' beyond the present, and knowing how far ahead prediction is required (see Section 3) the distance $d = x_B - x_A$ can found as,

$$d = t_P v_{gmx} \tag{25}$$

The distance at which the up-wave measurement is made is thus determined by the time into the future to which the wave profile needs to be predicted at the device location x_B. The wave profile measurement over $[0, T]$ where T is the present instant, thus contains information about the fastest traveling groups which will arrive at x_B at a time t_P into the future. On the other hand, for the slowest traveling groups also to arrive at x_B at time t_P into the future,

$$T + t_P = \frac{d}{v_{gmn}} \tag{26}$$

Eq. (26) can be used to determine T, the duration of measurement. Thus, if measurement begins at $t = 0$ and continues over $t > 0$, only at time $t = T$ does the prediction of wave profile at $(x_B, T + t_P)$ become available. Thereafter for all times $t > T$, the prediction at x_B is available for a time t_P seconds ahead, i.e. at $t + t_P$.

As Fig. 2 shows, $h_l(t) \neq 0$, $t < 0$ up to small values of $|t|$, i.e. h_l is non-causal [1]. This effect is due to the theoretical presence of frequencies $\omega < \omega_{mn}$. As seen from Eqs. (14) and (15), h_l is the result of an integral evaluated from $\omega \to 0$ to $\omega \to \infty$, As $\omega \to \infty$, $v_g \to 0$. However, as $\omega \to 0$, $v_g \to \infty$, which implies that disturbances occurring further up-wave, i.e. at $x < x_A$ influence the wave profile at x_B. Thus, it is not possible to obtain a causal h_l due to the theoretical presence of $\omega \to 0$. However, approximations using just the causal part of h_l and assuming $h_l(t) = 0$, $t < 0$ may still be reasonably effective for realistic wave spectra where the group velocities are expected to be within $v_{gmn} \leq v_g \leq v_{gmx}$ as defined above. With this reasoning, the present work also uses a causal approximation for

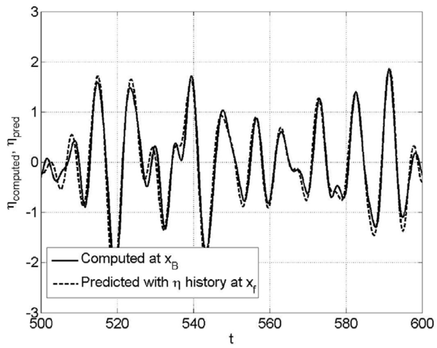

(a) $T_e = 11$ s, $H_s = 2.89$ m

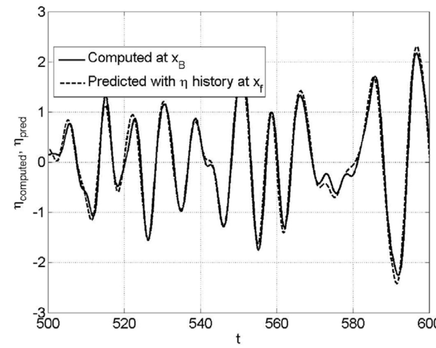

(b) $T_e = 13$ s, $H_s = 3.67$ m

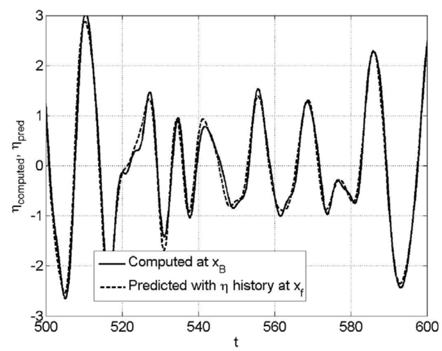

(c) $T_e = 15$ s, $H_s = 3.96$ m

Fig. 3. A comparison of the wave surface elevation at the device location as predicted $t_P = 30$ s into the future using the approach of Section 2 and as evaluated directly at the device location at $t + t_P$ seconds. $x_f = x_A$. The impulse response function h_l with its non-causal portion set to zero is used. Measurements at x_A, (a point 817.5 m up-wave) over $T = 232$ s and up to the present instant t are used in the convolution integral of Eq. (27) to arrive at a prediction at the device location at $t + t_P$.

$h_l(t)$ such that $h_l(t) = 0$, $t < 0$. Thus, for a chosen 'prediction interval' t_P ahead of the current time t,

$$\begin{aligned}
&\eta(x_B; t + t_p) = \int_0^T h_l(\tau)\eta(x_A; t - \tau)d\tau \\
&x_B - x_A = d = t_P v_{gmx} \\
&T = \frac{d}{v_{gmn}} - \frac{d}{v_{gmx}} \\
&t > T
\end{aligned} \tag{27}$$

where, as discussed, the up-wave measurement distance d is computed from the desired prediction time [see the paragraphs following Eqs. (63) and (67), and paragraphs 1 and 2 of Section 4] and the group velocity limit v_{gmx}. For irregular wave records derived from spectra with $T_e = 11$ s, $T_e = 13$ s, and $T_e = 15$ s, Fig. 3 shows the results using Eq. (27) with h_l as given by Eq. (21), except that $h_l(t) = 0$, $t < 0$ in Eq. (27) is used here. For $t_P = 30$ s, good agreement is found between $\eta(x_B; t + t_P)$ as predicted by Eq. (27) and the wave profile evaluated directly for the location x_B over time $t + t_P$, $t > T$.

3. Control force synthesis

The predicted wave surface elevation as given by Eq. (27) can be used to generate the desired hydrodynamically optimum velocity in the time domain in irregular waves. Small amplitude device oscillations are assumed. An axisymmetric omni-directional wave energy converter based on relative heave oscillation of two bodies is considered here, though the basic approach should apply to other devices with appropriate modifications. A schematic for the device is shown in Fig. 4. The analysis below is summarized from [47], and is included for completeness.

It should be noted that the assumption of linearity (small-amplitude incoming waves and small-amplitude device response) makes it possible to utilize linear superposition, and therefore to use first-order response kernels as the time-domain impulse response functions needed for wave-by-wave control. These time-domain impulse response functions can be derived via inverse Fourier transformation of the frequency–response functions and used in first-order convolutions to compute a time-series for arbitrary excitation (e.g. [50]). Such an approach was considered for time-domain ship-motion analysis using an integro-differential equation in [53], and later applied in the time-domain modeling and control of wave energy devices [23] (see also [1]). As mentioned, the actuator in the present work is assumed to be ideal and linear. Its response time constant is assumed to be short enough to enable any rapid changes in control forces as may be needed here. In addition, any stiction, saturation, and hysteretic effects are ignored. Furthermore, the oscillation constraints as applied here are not inequality constraints (as would frequently be associated with hard end stops). The control action does not consist of latching/declutching type braking or clutching forces, and the actuators are assumed to be capable for providing the required control force magnitudes. In the present situation therefore, it appears justifiable to model control implementation via force variations that are continuous and differentiable at all t. It is convenient then to begin with a frequency-domain description,

$$\begin{aligned}
&[Z_t(i\omega) + Z_L(i\omega)]v_t(i\omega) + [Z_c(i\omega) - Z_L(i\omega)]v_b(i\omega) = F_{ft}(i\omega) \\
&[Z_c(i\omega) - Z_L(i\omega)]v_t(i\omega) + [Z_b(i\omega) + Z_L(i\omega)]v_b(i\omega) = F_{fb}(i\omega)
\end{aligned} \tag{28}$$

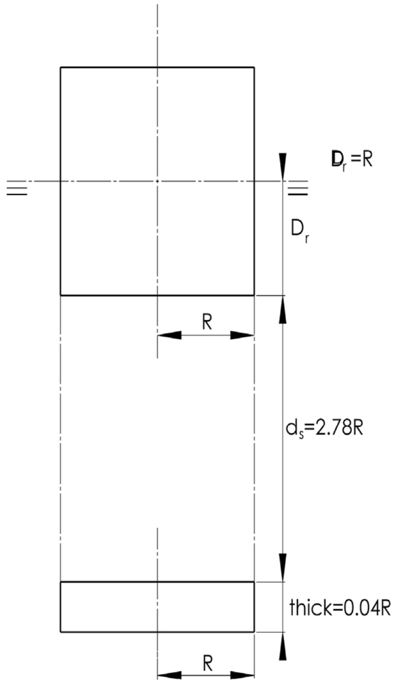

Fig. 4. The heaving axisymmetric device used in this work. Relative oscillation is used for energy conversion using a linear generator or hydraulic cylinder type power take-off mechanism/actuator, which is assumed to be linear and ideal (i.e. lossless). The power take-off also applies the required control force in this work, though in practice it may be advantageous to use two actuators, one for power take-off, and one for reactive forcing. The dimensions are based on the configuration studied in [52].

where the matrix elements are defined as,

$$\begin{aligned}
Z_t(i\omega) &= i\omega[m_t + \bar{a}_t(\infty) + a_t(\omega)] + \frac{k_t}{i\omega} + (c_{dt} + b_{dt}(\omega)) \\
Z_b(i\omega) &= i\omega[m_b + \bar{a}_b(\infty) + a_b(\omega)] + \frac{k_b}{i\omega} + (c_{db} + b_{db}(\omega)) \\
Z_c(i\omega) &= i\omega a_c(\omega) + b_c(\omega) \\
Z_L(i\omega) &= L(\omega) + \frac{N(\omega)}{i\omega}
\end{aligned} \tag{29}$$

where the letter m is used to denote in-air mass with the subscripts t and b respectively denoting the top and bottom bodies. b_{dt} and b_{db} denote the frequency-dependent radiation damping for the two bodies, while $\bar{a}_t(\infty)$ and $\bar{a}_b(\infty)$ denote the infinite-frequency added masses for the two bodies and $a_t(\omega)$ and $a_b(\omega)$ represent just the frequency-dependent parts of the respective added masses. The letter k denotes stiffness (hydrostatic for the floating buoy and mooring-related for the submerged disc), while c_{dt} and c_{db} represent the linearized viscous damping coefficients. a_c and b_c denote the frequency-variable added mass and radiation damping due to coupling between the two bodies. Z_L represents the load impedance applied by the power take-off on the relative oscillation. Following the approach of Falnes [46], it is possible to express Eq. (28) as a scalar equation in terms of the relative velocity $v_r(i\omega)$,

$$v_r(i\omega) = v_t(i\omega) - v_b(i\omega) \tag{30}$$

by defining,

$$\bar{Z}(i\omega) = Z_t(i\omega) + Z_b(i\omega) + 2Z_c(i\omega) \tag{31}$$

and

$$F_e(i\omega) = \frac{F_{ft}(i\omega)(Z_b(i\omega) + Z_c(i\omega))}{\bar{Z}(i\omega)} - \frac{F_{fb}(i\omega)(Z_t(i\omega) + Z_c(i\omega))}{\bar{Z}(i\omega)} \tag{32}$$

it is seen that

$$v_r(i\omega) = \frac{F_e(i\omega)}{Z_i(i\omega) + Z_L(i\omega)} \tag{33}$$

where

$$Z_i(i\omega) = \frac{Z(i\omega)Z_s(i\omega) - Z_c^2(i\omega)}{\bar{Z}(i\omega)} \tag{34}$$

For better accuracy in evaluating the hydrodynamic optimum relative velocity in the time domain and the control forces needed in approaching this optimum, it is convenient to separate the impedance terms into two parts, (i) a part consisting of the larger parameters m_t, m_b, k_t, k_b, $\bar{a}_t(\infty)$, and $\bar{a}_b(\infty)$, and (ii) a part consisting of the relatively smaller frequency-dependent radiation related effects. Thus,

$$\begin{aligned}
Z_t(i\omega) &= Z_{tu}(i\omega) + Z_{tnu}(i\omega) \\
Z_b(i\omega) &= Z_{bu}(i\omega) + Z_{bnu}(i\omega) \\
Z_L(i\omega) &= Z_{Lu}(i\omega) + Z_{Lnu}(i\omega)
\end{aligned} \tag{35}$$

where

$$\begin{aligned}
Z_{tu}(i\omega) &= i\omega[m_t + \bar{a}_t(\infty)] + k_t/i\omega \\
Z_{bu}(i\omega) &= i\omega[m_b + \bar{a}_b(\infty)] + k_b/i\omega
\end{aligned} \tag{36}$$

Note that $Z_{tu}(i\omega)$ and $Z_{bu}(i\omega)$ represent the large, inertial and stiffness impedances acting on the bodies. The linearized viscous damping c_{dt} and c_{db} are included in $Z_{tnu}(i\omega)$ and $Z_{bnu}(i\omega)$. The reactive forces dependent on $Z_{tu}(i\omega)$ and $Z_{bu}(i\omega)$ are determined using these impedances together with acceleration and displacement measurements. This leaves just the relatively smaller and c_d-related forces to be synthesized with convolutions and prevents any inaccuracies in the larger terms from dominating the inverse Fourier transformations needed in force evaluation. Eq. (28) can be re-written as,

$$[\mathbf{Z}_u(i\omega) + \mathbf{Z}_{Lu}]\mathbf{v}(i\omega) + [\mathbf{Z}_{nu}(i\omega) + \mathbf{Z}_{Lnu}(i\omega)]\mathbf{v}(i\omega) = \mathbf{F}(i\omega) \tag{37}$$

The load impedance component $\mathbf{Z}_{Lu}(i\omega)$ can then be chosen such that

$$[\mathbf{Z}_u(i\omega) + \mathbf{Z}_{Lu}(\omega)]\mathbf{v}(i\omega) = \mathbf{0} \tag{38}$$

which requires,

$$\frac{1}{Z_{Lu}(i\omega)} = -\left(\frac{1}{Z_{tu}(i\omega)} + \frac{1}{Z_{bu}(i\omega)}\right) \tag{39}$$

with $Z_{Lu}(i\omega)$ set to satisfy equation (39),

$$\begin{bmatrix} Z_{tnu}(i\omega) + Z_{Lnu}(i\omega) & Z_c(i\omega) - Z_{Lnu}(i\omega) \\ Z_c(i\omega) - Z_{Lnu}(i\omega) & Z_{bnu}(i\omega) + Z_{Lnu}(i\omega) \end{bmatrix} \begin{Bmatrix} v_t(i\omega) \\ v_b(i\omega) \end{Bmatrix} = \begin{Bmatrix} F_{ft}(i\omega) \\ F_{bt}(i\omega) \end{Bmatrix} \tag{40}$$

Now introducing $\bar{Z}_{nu}(i\omega)$ defined as

$$\bar{Z}_{nu}(i\omega) = Z_{tnu}(i\omega) + Z_{bnu}(i\omega) + 2Z_c(i\omega) \tag{41}$$

and

$$Z_{ni}(i\omega) = \frac{Z_{tnu}(i\omega)Z_{bnu}(i\omega) - Z_c^2(i\omega)}{\bar{Z}_{nu}(i\omega)} \tag{42}$$

and next redefining $F_e(i\omega)$ as

$$F_e(i\omega) = \frac{F_{ft}(i\omega)[Z_c(i\omega) + Z_{bnu}(i\omega)]}{\bar{Z}(i\omega)} - \frac{F_{fb}(i\omega)[Z_c(i\omega) + Z_{tnu}(i\omega)]}{\bar{Z}(i\omega)} \tag{43}$$

The relative velocity becomes,

$$v_r(i\omega) = \frac{F_e(i\omega)}{Z_{ni}(i\omega) + Z_{Lnu}(i\omega)} \tag{44}$$

Now $Z_{ni}(i\omega)$ can be expressed in terms of its real and imaginary parts, which are respectively, the equivalent hydrodynamic damping (i.e. radiation damping + linearized viscous damping) and reactance (arising from the frequency-dependent part of the equivalent added mass). Thus,

$$Z_{ni}(i\omega) = R_i(\omega) + iC_i(\omega) \tag{45}$$

$v_r(i\omega)$ is hydrodynamically optimum when

$$Z_{Lnu}(i\omega) = Z^*_{ni}(i\omega) \tag{46}$$

which leads to

$$v_{ro}(i\omega) = \frac{F_e(i\omega)}{2R_i(\omega)} \tag{47}$$

Limits on possible swept volume (i.e. before the floating buoy fully emerges from, or fully submerges into, water), and actuator stroke length dictate that displacement constraints be applied in practice. With α_r denoting the maximum relative displacement under constraint, at frequency ω, the velocity limit β_r is,

$$\beta_r = |i\omega\alpha_r| \tag{48}$$

The constraint requires,

$$v_r(i\omega)v^*_r(i\omega) \leq \beta_r^2 \tag{49}$$

Based on the method of Evans [38], satisfying the constraint (49) amounts to adding an effective damping term $\Lambda(\omega)$, which could be applied by the power take-off, such that

$$v_r(i\omega) = \frac{F_e(i\omega)}{2[R_i(\omega) + \Lambda(\omega)]} \tag{50}$$

The 'Lagrange multiplier' $\Lambda(\omega)$ can be found using

$$\Lambda(\omega) = \frac{|F_e(i\omega)|}{2\beta_r} - R_i(\omega) \tag{51}$$

It should be noted that applying the α_r constraint over $(-\omega_{mx}, \omega_{mx})$ limits the time-domain oscillation in response to a unit-impulsive wave elevation to,

$$s_r(t) = \frac{\alpha_r\omega_{mx}}{2\pi}\left(\frac{\sin\omega_{mx}t}{\omega_{mx}t}\right) \tag{52}$$

where $s_r(t)$ denotes the relative displacement. The functional form $\sin\omega_{mx}t/\omega_{mx}t \to 1$ as $t \to 0$. This function is also differentiable at $t \to 0$ (e.g. [54]). For $\omega_{mx} = \omega_h = \pi/2$ rad/s, and significant wave heights (H_s = 1–3 m) used in the calculations, as long as the instantaneous wave elevation encountered $\leq$4 m, the constraint as specified is also expected to be satisfied in the time domain.

The force applied by the actuator is

$$F_L(i\omega) = F_{Lu}(i\omega) + F_{Lnu}(i\omega) \tag{53}$$

where the causal part is,

$$F_{Lu}(i\omega) = -Z_{Lu}(i\omega)v_r(i\omega) \tag{54}$$

The following approach may be used to separate out components of $Z_{Lu}(i\omega)$ that are mass-like and stiffness-like. To find the stiffness-like component,

$$C_k = \lim_{\omega\to 0}\omega Z_u(i\omega) = \omega\frac{C_{tu}(\omega)C_{bu}(\omega)}{C_{tu}(\omega) + C_{bu}(\omega)} \tag{55}$$

To isolate the inertia-like load component,

$$C_m = \lim_{\omega\to\infty}\frac{1}{\omega}Z_u(i\omega) = \frac{1}{\omega}\frac{C_{tu}(\omega)C_{bu}(\omega)}{C_{tu}(\omega) + C_{bu}(\omega)} \tag{56}$$

The two limits in Eqs. (55) and (56) approach constant values, namely, the equivalent stiffness and inertia respectively. Then,

$$F_{Lu}(t) = C_m\dot{v}_r(t) + C_kx_r(t) \tag{57}$$

where the relative acceleration and displacement can be measured in real time using a combination of accelerometers and acoustic sensors. Note that this force is purely reactive and implies no net energy losses with ideal actuators. The following procedure is adopted for the synthesis of the remaining control forces. The exciting forces can be expressed in frequency domain as

$$\begin{aligned} F_{ft}(i\omega) &= H_{ft}(i\omega)\eta(x_B; i\omega) \\ F_{fb}(i\omega) &= H_{fb}(i\omega)\eta(x_B; i\omega) \end{aligned} \tag{58}$$

$H_{ft}(i\omega)$ and $H_{fb}(i\omega)$ are the exciting force frequency response functions for the individual bodies (evaluated for unit incident wave amplitudes at their respective centroids). $\eta(x_B; i\omega)$ denotes the incident free-surface elevation at the body centroid x_B. $F_e(i\omega)$ can then be expressed as

$$F_e(i\omega) = H_e(i\omega)\eta(x_B; i\omega) \tag{59}$$

where

$$H_e(i\omega) = \frac{H_{ft}(i\omega)[Z_c(i\omega) + Z_{bnu}(i\omega)]}{\bar{Z}_{nu}(i\omega)} - \frac{H_{fb}(i\omega)[Z_c(i\omega) + Z_{tnu}(i\omega)]}{\bar{Z}_{nu}(i\omega)} \tag{60}$$

Substitution of Eq. (59) into (47) gives

$$v_{ro}(i\omega) = \frac{H_e(i\omega)}{2R_i(\omega)}\eta(x_B; i\omega) \tag{61}$$

Taking the inverse Fourier transform of Eq. (61),

$$v_{ro}(t) = \int_{-\infty}^{\infty} h_o(\tau)\eta(x_B; t-\tau)d\tau \tag{62}$$

where

$$h_o(t) = \frac{1}{2\pi}\int_{-\infty}^{\infty}\frac{H_e(i\omega)}{2R_i(\omega)}e^{i\omega t}d\omega \tag{63}$$

$h_o(t)$ is non-causal, as shown in Fig. 5 for the 2-body device in Fig. 4. However, for $t<0$, $h_o(t)$ can be truncated as $t \to -t_p$, where in the present case $t_p \approx 15$ s. The velocity $v_{ro}(t)$ can be used to synthesize the control forces to be applied as seen below. This type of feed-forward control can be supplemented by a feedback control loop to correct for errors due to measurement errors and other small unmodeled effects. Such an inner loop is not included in the present work. From Eq. (46), in the absence of oscillation constraints, the control force can be expressed in the frequency domain as

$$F_{Lnu}(i\omega) = Z^*_{ni}(i\omega)v_{ro}(i\omega) \tag{64}$$

Letting $Z^*_{ni}(i\omega) = R_i(i\omega) + iC_i(i\omega)$, and using Eq. (61),

$$F_{Lnu}(i\omega) = \left[\frac{H_e(i\omega)}{2} + i\frac{C_i(\omega)H_e(i\omega)}{2R_i(\omega)}\right]\eta(x_B; i\omega) \tag{65}$$

Two impulse response functions $h_{ri}(t)$ and $h_{ci}(t)$ can be defined such that,

$$F_{Lnu}(t) = \int_{-\infty}^{\infty} h_{ri}(\tau)\eta(x_B; t-\tau)d\tau + \int_{-\infty}^{\infty} h_{ci}(\tau)\eta(x_B; t-\tau)d\tau \tag{66}$$

where

$$\begin{aligned} h_{ri}(t) &= \frac{1}{2\pi}\int_{-\infty}^{\infty}\frac{H_e(i\omega)}{2}e^{i\omega t}d\omega \\ h_{ci}(t) &= \frac{1}{2\pi}\int_{-\infty}^{\infty}\frac{H_e(i\omega)C_i(\omega)}{2R_i(\omega)}e^{i\omega t}d\omega \end{aligned} \tag{67}$$

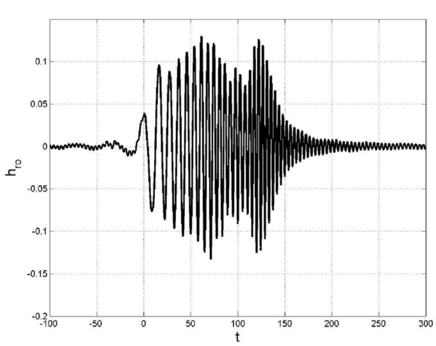

(a) Impulse response function h_o

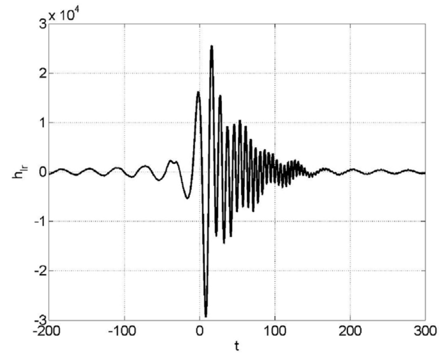

(b) Impulse response function h_{ri}

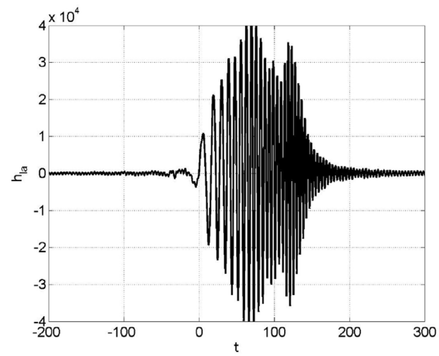

(c) Impulse response function h_{ci}

Fig. 5. The impulse response function h_o as obtained using Eq. (18) which defines the hydrodynamically near-optimum variation for the relative velocity, shown along with the two impulse response functions used to determine the control force to be applied by the actuator. h_{ri} is used to find the resistive part of this force, while h_{ci} is used to find the reactive part. All three impulse response functions are non-causal as discussed, necessitating the use of the predicted wave profiles evaluated here.

Fig. 5 shows the impulse response functions $h_{ri}(t)$ and $h_{ci}(t)$. It is seen again that h_{ci} and $h_{ri}(t)$ are non-causal. However, for $t<0$, $h_{ci}(t)$ can be truncated as $t \to -t_c$ where $t_c = 30$ s. The actual prediction time ahead $t_P \equiv t_T$ here can be chosen to be $\max(t_p, t_c)$, and is chosen to be $t_T = 30$ s. With the control force $F_{Lnu}(t)$ applied, the actual relative velocity can be found as

$$v_{ract}(t) = \int_{-\infty}^{\infty} h_A(\tau)\eta(x_B; t-\tau)d\tau + \int_{-\infty}^{\infty} h_R(\tau)\eta(x_B; t-\tau)d\tau \quad (68)$$

where

$$h_A(t) = \frac{1}{2\pi}\int_{-\infty}^{\infty} \frac{H_e(i\omega)}{Z_{ni}(i\omega)} e^{i\omega t} d\omega$$
$$h_R(t) = \frac{1}{2}\int_{-\infty}^{\infty} \frac{[iC_i(\omega) - R_i(\omega)]H_e(i\omega)}{2R_i(\omega)Z_{ni}(i\omega)} e^{i\omega t} d\omega \quad (69)$$

In the present work, all of the integrals in Eqs. (67) and (69) were evaluated from $-t_T$ to the present time t where all of the impulse response functions were truncated at $t = -30$ s. This meant that $\eta(x_B\,;t)$ was to be predicted $t_T = 30$ s into the future. Recall that this prediction was described in the discussion leading up to Fig. 3.

Representing the two terms comprising $F_{Lnu}(t)$ in Eq. (66) as $F_l(t)$ and $F_a(t)$, it is observed that $F_l(t)$ is derived from the resistive part of the impedance R_i, and F_a from the reactive part C_i. Net power absorption is therefore due to F_l, while F_a exchanges reactive power with the device. Thus,

$$F_l(t) = \int_{-\infty}^{\infty} h_{ri}(\tau)\eta(x_B; t-\tau)d\tau$$
$$F_a(t) = \int_{-\infty}^{\infty} h_{ci}(\tau)\eta(x_B; t-\tau)d\tau \quad (70)$$

To find the forces in the presence of oscillation constraints, $R_i(\omega)$ in Eqs. (47), (61), (65), (67) and (69) is replaced by $R_i(\omega) + \Lambda(\omega)$. Note that these integrals in the present work are evaluated from $-t_T$ to the present time t, and $\eta(x_B\,;t)$ is predicted t_T beyond the present time t.

With and without the oscillation constraint present, the average power absorbed over a time period $[0, T]$ can be found using

$$P_w = \frac{1}{T}\int_0^T F_l(t)v_{ract}(t)dt \quad (71)$$

On the other hand, the instantaneous reactive power can be computed using,

$$P_a = F_a(t)v_{ract}(t) \quad (72)$$

The average incident power in a wave crest of unit length (in kW) in a spectrum of long crested waves at significant wave height H_s and energy period T_e is given by

$$P_{in} = 0.49H_s^2T_e \quad (73)$$

An energy capture length ℓ can then be defined as

$$\ell = \frac{P_w}{P_{in}} \quad (74)$$

These results are compared with the approximate near-optimal control results based on up-wave measurements at 2 points as described in [47].

4. Calculations

As mentioned, the geometry shown in Fig. 4 is used in the calculations. The choice of the device and the geometry affects the lengths of the radiation impulse response function and the excitation force kernel; and consequently also the up-wave distance, measurement interval, and the prediction time. No particular effort was made here to optimize the geometry or device choice from this standpoint. The geometry here was chosen to match that analyzed in [52], and the hydrodynamic parameter variations reported therein were used in the present calculations (the effect of the tube in [52] was ignored). Buoy and disc radii were taken to be $R=8$ m, with the buoy draft $D_r=R$. As mentioned, this is the geometry for which the impulse response functions are shown in Fig. 5. Recall that h_{ri} and h_{ci} for $t<0$ can be truncated at $-t_c=-30$ s, while h_o can be truncated at $-t_p=-15$ s.

As mentioned, the greater of the two truncation times, namely, $t_T=\max(t_c, t_p)$ was used here as the prediction time $t_P=t_T$ in all of the force and response calculations (it was verified that using this value rather than $t_p=15$ s for the optimum velocity calculation had a negligible effect). As mentioned, long-crested 2-parameter irregular wave spectra were assumed. It was thought to be reasonable to truncate the spectral density variation over $\omega_l \leq 0.18$ rad/s and $\omega_h \geq 1.57$ rad/s. Deep water conditions were assumed. This meant that $v_{gmn}=3.124$ m/s, and $v_{gmx}=27.25$ m/s.

Based on Eqs. (25) and (26), these conditions lead to $d=817.5$ m, and $T=232$ s. Thus, wave elevation measurements should be made at a point approximately 817 m up-wave, and over a time duration $T=232$ s.

For the long-crested, 2-parameter spectra used in this work (Eq. (75)), the surface elevation at $x=x_A$ was found using Eq. (76).

$$S(\omega)=\frac{131.5H_s^2}{T_e^4\omega^5}\exp\left[-\frac{1054}{(T_e\omega)^4}\right] \tag{75}$$

$$\eta(x_A;t)=\sum_{n=1}^{N}\Re\{A(\omega_n)\exp[-i(k(\omega_n)x_A-\omega_n t+\theta_n)]\} \tag{76}$$

where

$$A(\omega_n)=\sqrt{2S(\omega_n)\Delta\omega} \tag{77}$$

and θ_n is a random number $\in[0, 2\pi]$, with $S(\omega_n)$ representing the spectral density value at ω_n. $N=512$ was used in these calculations. For direct evaluation of η at x_B, the same ω_n, θ and $A(\omega_n)$ were used to compute $\eta(x_B;t)$ as

$$\eta(x_B;t)=\sum_{n=1}^{N}\Re\{A(\omega_n)\exp[i(-k(\omega_n)x_B-\omega_n t+\theta_n)]\} \tag{78}$$

A program was developed within Matlab to provide the wave prediction at the device centroid using up-wave elevation measurements over $T=232$ s at x_A located $d=817.5$ m up-wave. The predicted wave profile was then supplied to the program that computed the control forces, the resulting relative velocity, and average absorbed power based on Eqs. (70), (68) and (71). Oscillation constraints could be turned on and off within this routine. Calculations were carried out over [0, 1300] s, though control and power absorption was only applied after the predicted wave elevation at the device became available. Results from this routine over a range of spectra were collected and plotted in the overview plots discussed in the following section.

5. Discussion of results

As mentioned, this work uses wave surface elevation measurements over a duration of time some distance up-wave of the device to compute the wave elevation up to a certain time into the future for the purpose of evaluating the instantaneous actuator force required to approach hydrodynamically optimum velocity on a wave-by-wave basis. Long-crested, small amplitude waves are assumed, and device oscillation amplitudes are also assumed to be small. Thus, linear theory is used at all stages. The main results are discussed below.

The impulse response functions h_{ri} and h_{ci} in Fig. 5 can be truncated at $t=-30$ s, in the $t<0$ range. This helps to determine one of the values on the space time diagrams of Fig. 1, namely, the time beyond the present instant at which the predicted wave surface elevation is required. The group velocity limits v_{gmx} and v_{gmn} can be based on frequency limits ω_l and ω_h that are likely to encompass most expected spectra at the device site. The prediction time t_T here and the maximum group velocity v_{gmx} determine the distance up-wave at which the wave measurement should be made. The minimum group velocity v_{gmn} then determines the length of time T over which the measurement needs to be acquired. Recall that Fig. 2 shows the impulse response function describing the propagation of an impulsive excitation, although the non-causal part is ignored in the calculations. The distance at which measurement is made is $d=817.5$ m, which may be regarded as acceptable for a deterministic propagation model [1]. Measurements are recorded for $T=232$ s as mentioned above in order to obtain a prediction at the device location $t_T=30$ s into the future.

The plots of Fig. 3 compare the wave elevation as computed directly for the position x_B with that predicted using the present prediction approach. The root-mean-square errors observed are on the order of 8×10^{-2} m, which is about 5–7% of the root-mean-square elevation. The chosen cut-off frequency values of ω_l and ω_h in relation to the approximation of causality for the impulse response function h_l, may be one of the factors responsible for the errors, with frequency and time domain discretization errors being a smaller contributor. Given the overall approximation implicit in adopting the linear theory framework, these prediction errors observed here may be considered acceptable.

It should be noted that the device location and the wave rider buoy location may not be precisely known in practice, because both will be moored structures, and as such, subject to position variation within their respective 'watch circles'. The present treatment assumes 'nominal' locations, and it should be recognized that predictions based on the nominal distances will be within uncertainty bands dictated by the sensitivity of the predictions to the distance parameter d. This point needs to be examined further in future work, though it may be noted that it is not too difficult to choose the prediction time to be greater than required by the impulse response functions, although this would come at the cost of additional computational time and errors. As long as the prediction time is chosen to be greater than t_T (=30 s in the present case), it may be worth considering choosing the prediction time to accommodate the worst-case situation within watch circles.

The effect of errors in the up-wave measurements on the predicted wave elevation of Eq. (27) and the resistive and reactive forces of Eq. (70) is examined below. Such errors could come from the additional presence of small short-crested waves, instrument error, etc.

Letting $\eta_m(x_A;t)$ denote the wave elevation measurement at x_A, and $\varepsilon(x_A;t)$ the error, the relationship between the correct value $\eta(x_A;t)$ and the measurement can be expressed as

$$\eta_m(x_A;t)=\eta(x_A;t)+\varepsilon(x_A;t) \tag{79}$$

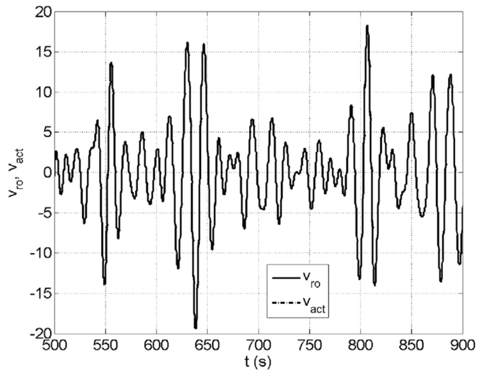

(a) Unconstrained Oscillation

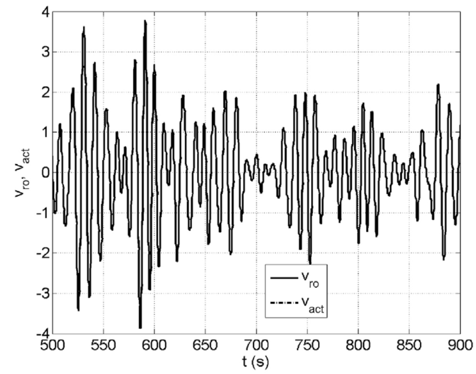

(b) Relative Oscillation $\leq D_r/2$

Fig. 6. The relative heave velocity between the buoy and the disc for a spectrum with T_e = 13 s and H_s = 3.0 m. (a) Shows unconstrained oscillation, while (b) shows a case where relative oscillation amplitude is constrained to be within $D_r/42$ (1/2 the buoy draft). The near-optimum in each case is closely matched by the velocity produced on application of the actuator (control) force. In practice, there will be differences due to model uncertainties, measurement errors, and other disturbances. An inner feedback loop would be required to ensure a close match. This work only considers the effect of the feedforward force.

Use of this measurement in Eq. (27) will provide an estimate $\eta_e(x_B\,; t+t_p)$,

$$\eta_e(x_B; t+t_p) = \int_0^T h_l(\tau)\eta_m(x_A; t-\tau)d\tau \tag{80}$$

Inserting Eq. (79) into Eq. (80), it can be seen that (the present first-order convolution operation being linear),

$$\eta_e(x_B; t) = \eta(x_B; t+t_p) + \varepsilon(x_B; t+t_p) \tag{81}$$

where

$$\varepsilon(x_B; t+t_p) = \int_0^T h_l(\tau)\varepsilon(x_A; t-\tau)d\tau \tag{82}$$

Errors $\varepsilon(x_A\,; t)$ will also propagate into the resistive and reactive control forces to be applied. Denoting the instantaneous error in the resistive force $F_l(t)$ as $\varepsilon_l(t)$, it can be verified that

$$\varepsilon_l(t) = \int_{-\infty}^{\infty} h_{ri}(\tau)\varepsilon(x_B; t-\tau)d\tau \tag{83}$$

Similarly, the error $\varepsilon_a(t)$ in the reactive force $F_a(t)$ can be expressed as

$$\varepsilon_a(t) = \int_{-\infty}^{\infty} h_{ci}(\tau)\varepsilon(x_B; t-\tau)d\tau \tag{84}$$

As before, the integrals may be evaluated from $-t_T$ where h_{ri} and h_{ci} can be truncated to the present time t, with $\eta(x_B\,; t)$ predicted up to t_T beyond t.

Since h_l in Eq. (82) represents the propagation impulse-response function such that $\eta(x_A\,; t)$ and $\eta(x_B\,; t+t_p)$ are the same order of magnitude, $\varepsilon(x_B\,; t+t_p)$ must be the same order of magnitude as $\varepsilon(x_A\,; t)$. A 10% error in wave-profile measurement at x_A could thus be expected to result in a 10% error in the predicted wave elevation at x_B, as well as in the forces F_l and F_a, according to Eqs. (83) and (84). Therefore, if the wave measurements are known to contain large errors, some type of real-time digital filtering technique (to minimize their propagation into the prediction) may be warranted, providing it does not add signal delays. With the same caveat, more elaborate Kalman filtering algorithms built around the present deterministic propagation model may also be worth considering.

Fig. 6 plots the relative heave velocity under near-optimal control. It is found that the velocity as given by Eq. (68) matches the desired optimum velocity closely, both without and in the presence of an oscillation constraint where maximum amplitude of relative oscillation is restricted to be $\leq D_r/2$. In an experimental implementation, a greater deviation may be expected due to model inaccuracies and measurement errors. A trajectory tracking feedback controller may then be added in order to minimize the velocity and position tracking errors.

Fig. 7 plots the absorbed power variation for a spectrum with H_s = 3.0 m, T_e = 13 s with the relative oscillation amplitude constrained to be $\leq D_r/2$. The average absorbed power over 10 min is ≈96 kW. Note that the overall system may be designed to stop operation and enter survival mode in wave climates with $H_s \geq 5$ m. Further, there may be a further constraint on actuator operation due to force limitations. This has not been considered here. Recall that oscillation constraints are here imposed using the formulation of [38], as summarized in Eqs. (50) and (51). It should also be noted that actuator operation is assumed to be ideal here, in that any power dissipation within the actuator is ignored. This assumption also has relevance to Fig. 8, which shows the variation of the reactive power to be supplied by the actuator in order to bring about control as discussed in this work. Although the average reactive power spent in achieving control is zero (within numerical accuracy) in this case, net energy would need to be spent in achieving such control for non-ideal actuators (e.g. [10]). Notably, however, the maximum reactive power magnitude in Fig. 8 is comparable to

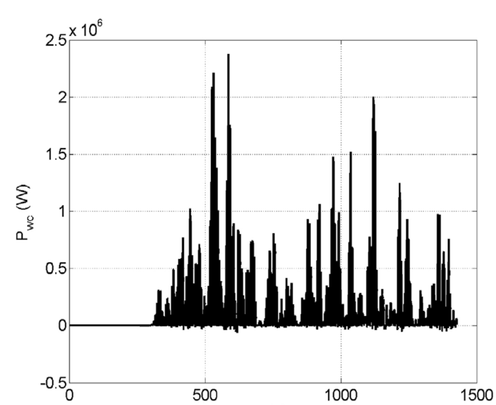

Fig. 7. Instantaneous absorbed power variation for a spectrum with T_e = 13 s and H_s = 3.0 m. Actuator force is applied after $t = T$ s, and instantaneous power is computed using Eq. (71). Displacement constraint is applied following the technique of [38] as described in Section 2. The average power over the time window of observation above under these wave conditions is 96 kW. The force F_l is applied on the relative oscillation.

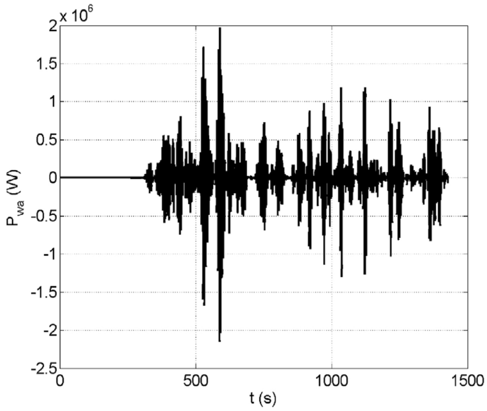

Fig. 8. Instantaneous reactive power variation for a spectrum with $T_e = 13$ s and $H_s = 3.0$ m. Actuator force F_a is applied after $t = T$ seconds, and instantaneous power is computed using Eq. (72). Displacement constraint is applied following the technique of [38] as described in Section 2. An ideal actuator is assumed, so that no net energy is lost in the actuator during reactive force application. The average reactive power over the time window of observation above under these wave conditions is zero within numerical errors. The force F_a is reactive and is applied on the relative oscillation.

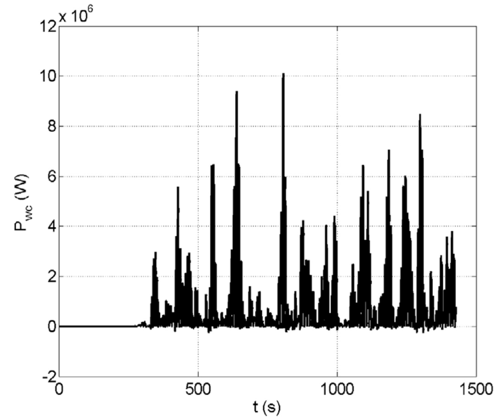

Fig. 10. Instantaneous absorbed power variation without oscillation constraints for a spectrum with $T_e = 13$ s and $H_s = 3.0$ m. Actuator force is applied after $t = T$ seconds, and instantaneous power is computed using Eq. (71). The average power over the time window of observation above under these wave conditions is 750 kW. As before, the force F_l is applied on the relative oscillation.

the maximum absorbed power magnitude in the conditions studied in these figures. Therefore, short term on-board energy storage only may be adequate here.

Fig. 9 plots the force variations $F_l(t)$ and $F_a(t)$ for the spectrum with $T_e = 13$ s, $H_s = 3.0$ m. It should be noted that F_a is a part of the total reactive force needed, and that the total reactive force requirement is expected to be greater. A systematic design effort/study would be needed in order to achieve a better balance between the resistive and reactive force components needed in control (e.g. by extending an approach such as discussed in [55]). The overall design would likely be a trade between device size and actuator technology (in terms of deliverable force and power dissipation).

For comparison with Fig. 7, Fig. 10 plots the absorbed power variation associated with unconstrained oscillation for this device. The average absorbed power over 10 min is found to be ≈750 kW for a spectrum with $H_s = 3.0$ m and $T_e = 13$ s.

It is informative to compare the performance of the present approach with a sub-optimal strategy based on a single group velocity ('approximate near-optimal control'). Results utilizing this approach were included in a recent paper [47]. Acknowledging that in practical situations it is the behavior under oscillation constraints that should be the focus, Fig. 11 compares the capture width available with the two strategies under an oscillation constraint $\leq D_r/2$ in irregular waves, for spectra from $T_e = 6$ s to $T_e = 17$ s, $H_s = 1.0$ m. It is observed that the present approach performs up to 5 times better than the approximate approach under the prescribed constraint. Results of single runs are shown here. The run-to-run variation due to random phase mixing appears to be greater for the full near optimal control runs. This could be a result of the particular numerical procedures used for the two cases. Specifically, the number of frequency components used was smaller in the full near optimal procedure to save calculation time (given that this procedure also included the full wave prediction component). Notwithstanding this, the difference between the capture widths for the two strategies exceeds the variability seen in the full near-optimal plot, and considerably greater absorption is observed under near-optimal control based on full prediction. To understand the difference in terms of absorbed power, $H_s = 1.0$ m was used with the entire range of T_e values to obtain Fig. 12. Over 4 times as much power is seen to be absorbed with full near-optimal control.

Fig. 13 compares the F_l and F_a force maxima over the spectral T_e range covered here, for $H_s = 1$ m. The results are obtained for an oscillation constraint $D_r/4$, for which the velocity remains at the maximum allowed for a significant portion of the T_e range. In

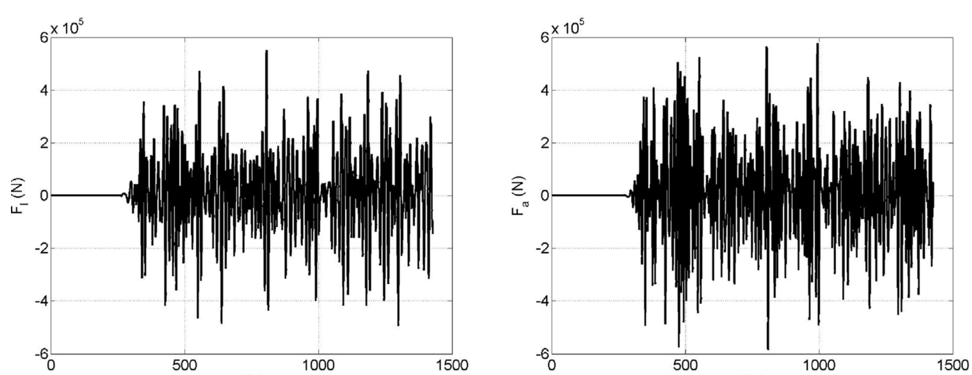

(a) Resistive Force F_l

(b) Reactive Force F_a

Fig. 9. The resistive and reactive forces to be applied by the actuator in a spectrum with $T_e = 13$ s and $H_s = 3.0$ m. (a) Shows the power absorbing resistive force, while (b) shows the reactive force needed. The relative oscillation amplitude is constrained to be within $D_r/2$ (1/2 the buoy draft). Overall, the F_a maxima are seen to be larger than those of the force F_l even though the difference is less than an order of magnitude. It should be noted that F_a does not include the contribution of the force applied according to Eq. (39). Actuation is assumed to be ideal and lossless, and nonlinearities in the actuator are ignored.

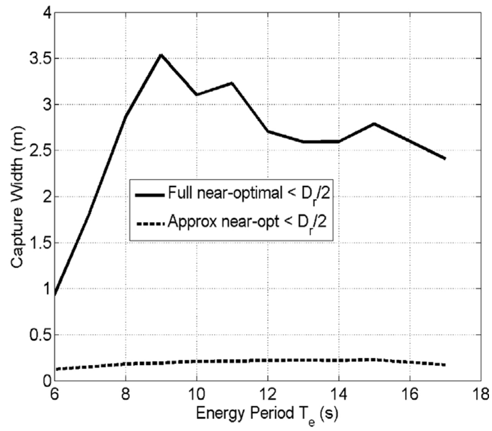

Fig. 11. Power capture length as a ratio of averaged absorbed power over the simulation duration and the average incident power per unit crest length. Oscillations are constrained to $D_r/2$. Results are compared with the approach of [47], recomputed for the constraint $D_r/2$. As pointed out in the text, results from single runs are plotted here (rather than results averaged over several runs), and the results with full near-optimal control are more sensitive to run-to-run differences in the irregular wave signals generated each time.

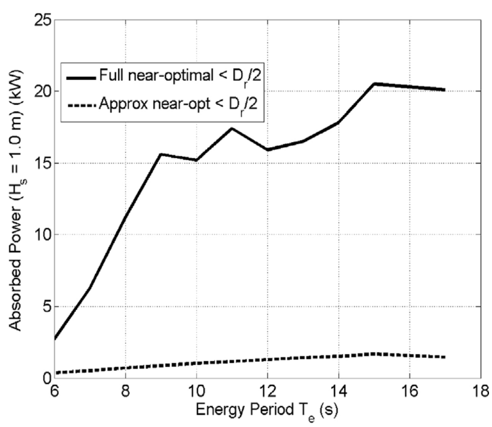

Fig. 12. Average absorbed power with the oscillations constrained to $D_r/2$. Power calculations use a nominal H_s of 1.0 m for each energy period. Results are compared with the approach of [47], recomputed for the constraint $D_r/2$. As pointed out in the text, the results with full near-optimal control are more sensitive to run-to-run differences in the irregular wave signals generated each time.

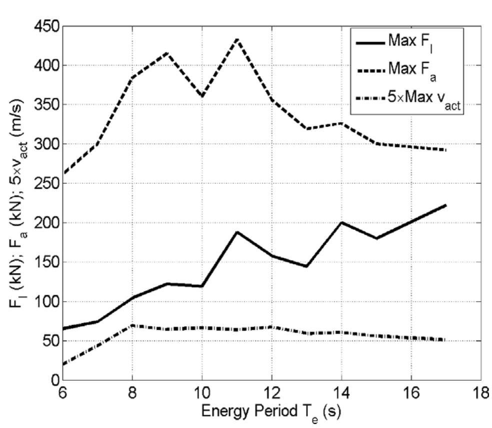

Fig. 13. The variation of the maxima for the forces F_l and F_a shown together with the velocity maximum for the spectra considered here. In all spectra, H_s = 1 m, with T_e as shown on the x-axis. Oscillations are constrained to $D_r/4$. For the present device, F_a is seen to dominate F_l over the entire energy-period range. Part of the resistive force is needed as constraint force through the Λ term in Eq. (50), and greater constraint force is required to meet the constraint in spectra with the longer T_e. F_a is part of the reactive force necessary. The oscillation constraints are expected to limit the total reactive force the same way as they limit F_a as T_e increases.

the longer T_e range, the velocity limit increases the F_l requirement since F_l also provides the constraint through Λ. However, the velocity constraint does also limit the F_a requirement in the swell-rich longer T_e range. Although F_a is only a part of the total reactive force needed and the overall reactive force requirement will likely be greater, it would still be limited indirectly by the velocity constraint. A more detailed study of the reactive and resistive forces in relation to device geometry and actuator technology seems warranted, in order to gain a better understanding of the hardware requirements of present control approach.

When device operation is amplitude-limited as under oscillation constraints, it becomes important to make the best use of the excitation at small and moderate amplitudes. Control that enables a closer approach to the time-domain optimum velocity can make better use of available wave-by-wave excitation, and is therefore more effective under oscillation constraints than approaches based on approximations such as implicit in the assumption of single-group velocity propagation.

It should be noted that no additional measurement hardware is required in migrating from approximate approaches utilizing a single, non-dispersive group velocity to a more accurate approach that uses a more complete propagation model based on a range of group velocities in representative realistic spectra. The additional improvement in the absorbed power appears to be primarily a result of a more accurate prediction algorithm. The computational efficiency of the prediction algorithm is not considered a potential limitation in this work, and it is assumed that adequate computing hardware can be found that is capable of processing the additional calculation without difficulty, so that the actuator can receive the necessary signals in real time. If the shortest wave periods of interest in practice are close to 4 or 5 s, then these would likely drive the sampling and calculation interval limits in practice. In this work, both F_l and F_a are thought to be provided by the same actuator. However, from a practical standpoint, use of two different actuators for the two types of forces would probably be preferable. In this regard, experimental testing of the overall procedure and its effect on energy capture should provide valuable experience.

Finally, this work assumes that the incoming waves are long-crested or uni-directional. Extensions to multi-directional seas may be possible with directionally spread up-wave measurement if small-amplitude waves and linear superposition are assumed. A combination of spatially distributed sampling (such as based on a radar system) along with point-based measurement over the required time duration may be needed, and the additional cost of obtaining such measurements (including cost of additional power required to operate the hardware) would need to be considered case by case.

6. Conclusion

The goal of this work was to investigate the effect of a deterministic propagation model based approach to incident wave prediction that accounted for a range of group velocities, for the purpose of wave-by-wave control of a wave energy device. Linear wave propagation and linear system response were assumed, so that the results are limited to small-amplitude oscillations in small-amplitude waves. Uni-directional/long-crested waves were assumed, and further, heave motion was assumed to be the dominant mode for a 2-body axisymmetric device. Viscous effects were assumed to be small and linear, and an ideal power take-off with a linear response and negligible dissipation was assumed. Wave prediction at the device centroid was obtained using surface elevation measurements at an up-wave distance and over a measurement duration computed knowing the prediction time ahead and the range of group velocities representative of the frequency content in realistic spectra. The prediction time was determined using impulse response functions describing the control forces to be applied on the relative heave oscillation. Due to linearity, it was straightforward to express the control force as a convolution of an impulse response function with respect to the predicted wave surface elevation (t_T seconds ahead of the current instant) at the device centroid *G*. Thus, wave measurements over a forward-moving time window up to the present instant (from $t-T$ to t) were used to generate a prediction $t+t_T$ over the calculation time interval.

Results showed considerable improvement over approximate control based on up-wave measurement that assumes propagation at a single group velocity. Average power absorption both without and with constraints on the relative oscillation between the buoy and the disc showed an increase over a wide range of energy-period T_e values. It should be noted that oscillation amplitudes close to the hydrodynamic velocity optimum can become too large (i) for the assumptions of linearity to remain valid, and (ii) for the device to be able to support, given its draft and above-water geometry and/or mechanical limits of the power take-off. Of particular note here is the increase in absorption under highly restrictive oscillation constraints. Force limits were not considered explicitly, and it would be worthwhile to study the effect of force constraints in addition to oscillation amplitude constraints on the power absorption with this approach. Providing the chosen actuators are able to apply the required resistive and reactive loads, and are designed to minimize internal dissipation, based on the present results, it appears reasonable to propose that a control approach utilizing the hydrodynamic fundamentals of deterministic wave propagation and device response modeling would enable considerable enhancement in small-amplitude irregular waves under oscillation constraints. The device used here was an axisymmetric heaving 2-body system where the relative oscillation between a floating cylindrical buoy and a submerged circular disc enabled energy conversion.

Pierson–Moskowitz type 2-parameter spectra were used here. While these spectra were uni-modal, there does not appear to be an *a-priori* reason precluding the application of the present approach in multi-modal spectra. Further work could include a generalization of the present approach to include multiple-mode oscillation, directional incident waves, and force-limited actuators. Especially for larger omni-directional converters or crest-spanning devices, 2-point up-wave measurement may be required for the separation of the incident wave field from the diffracted and radiated wave fields. The current propagation model assumes linearity and does not account for changes due to wind action between the measurement location and the device position. Finally, new device configurations that provide a better balance between the resistive and reactive forces required in the present control approach may be worth considering. In addition, it may also be particularly worthwhile to investigate actuator designs that provide increased forces at a minimal power loss so that the potential gains from control can be realized in practice.

Acknowledgements

I thank Larry and Linda Pearson and the SDSM&T Foundation for their support through the Pearson endowment. I also thank the reviewers of this paper for their helpful suggestions.

References

[1] Falnes J. On non-causal impulse response functions related to propagating water waves. Appl Ocean Res 1995;17(6):379–89.
[2] McCormick ME. Ocean wave energy conversion. NY: John Wiley and Sons; 1981 [reissued with revisions, 2007, Dover, NY].
[3] Salter SH. Wave power. Nature 1974, June:720–4.
[4] Falcao AFO. Wave energy utilization: a review of the technologies. Renew Sustain Energy Rev 2010;14:899–918.
[5] Salter SH. Development of the duck concept. In: Proc wave energy conference. 1978.
[6] Budal K, Falnes J. Optimum operation of improved wave power converter. Mar Sci Commun 1977;3:133–50.
[7] Budal K, Falnes J. Interacting point absorbers with controlled motion. In: Count BM, editor. Power from sea waves. London: Academic Press; 1980. p. 381–99.
[8] Ringwood JV, Bacelli G, Fusco F. Energy-maximizing control of wave-energy converters. In: IEEE control systems magazine. 2014, October. p. 30–55.
[9] Hoskin RE, Count BM, Nichols NK, Nicol DAC. Phase control for the oscillating water column. In: Evans DV, Falcão AFdeO, editors. Proc IUTAM symp hydrodynamics of wave energy utilization. Berlin: Springer Verlag; 1985. p. 257–68.
[10] Perdigao JNBA, Sarmento AJNA. A phase control strategy for OWC devices in irregular waves. In: Grue J, editor. Proc 4th international workshop on water waves and floating bodies. 1989. p. 205–9.
[11] Falcao AFO, Justino PAP. OWC wave energy devices with air flow control. Ocean Eng 1999;127:5–1295.
[12] Falcao AFO. Phase control through load control of oscillating body wave energy converters with hydraulic PTO system. Ocean Eng 2008;35:358–66.
[13] Korde UA. Phase control of floating bodies from an on-board reference. Appl Ocean Res 2001;23:251–62.
[14] Babarit A, Clement AH. Optimal latching control of a wave energy device in regular and irregular waves. Appl Ocean Res 2006;28(2):77–91.
[15] Salter SH, Taylor JRM, Caldwell NJ. Power conversion mechanisms for wave energy. Proc Inst Mech Eng M: J Eng Marit Environ 2002;216:1–27.
[16] Babarit A, Guglielmi M, Clement AH. Declutching control of a wave energy converter. Ocean Eng 2009;36:1015–24.
[17] Skyner D. Solo duck linear analysis. Technical report. University of Edinburgh; 1987.
[18] Nebel P. Maximizing the efficiency of wave-energy plants using complex conjugate control. Proc IMechE I – J Syst Control Eng 1992;206(4):225–36.
[19] Korde UA. A power take-off mechanism for maximizing the performance of an oscillating water column wave energy device. Appl Ocean Res 1991;13(2):75–81.
[20] Hansen RH, Kramer MM. Modeling and control of the wave star prototype. In: Proc 9th European wave and tidal energy conference. 2011 [paper 163].
[21] Jeffreys ER. Simulation of wave power devices. Appl Ocean Res 1984;6(1):31–9.
[22] Wehausen JV. Causality and the radiation condition. J Eng Math 1992;26:153–8.
[23] Naito S, Nakamura S. Wave energy absorption in irregular waves by feedforward control system. In: Evans DV, Falcão AFdeO, editors. Proc IUTAM symp hydrodynamics of wave energy utilization. Berlin: Springer Verlag; 1985. p. 269–80.
[24] Korde UA. Efficient primary energy conversion in irregular waves. Ocean Eng 1999;26:625–51.
[25] Korde UA, Schoen MP, Lin F. Strategies for time-domain control of wave energy devices in irregular waves. In: Proc 11th Int Soc Offshore and Polar Engr (ISOPE) Conference. 2002.
[26] Fusco F, Ringwood JV. A study of the prediction requirements in real-time control of wave energy converters. IEEE Trans Sustain Energy 2012;3(1):176–84.
[27] Hals J, Falnes J, Moan T. Constrained optimal control of a heaving buoy wave energy converter. J Offshore Mech Arct Eng 2011;133(1):1–15.
[28] Fusco F, Ringwood JV. A simple and effective real-time controller for wave energy converters. IEEE Trans Sustain Energy 2013;4(1):21–30.
[29] Fusco F, Ringwood JV. A hierarchical robust control of oscillating wave energy converters with uncertain dynamics. IEEE Trans Sustain Energy 2014;5(3):958–66.
[30] Scruggs JT, Lattanzio SM, Taflanidis AA, Cassidy II. Optimal causal control of a wave energy converter in a random sea. Appl Ocean Res 2013;42:1–15.
[31] Hals J, Falnes J, Moan T. A comparison of selected strategies for adaptive control of wave energy converters. J Offshore Mech Arct Eng 2011;133(3):1–12.
[32] Korde UA. On a near-optimal control approach for a wave energy converter in irregular waves. Appl Ocean Res 2014;46:79–93.
[33] Cretel JAM, Lightbody G, Thomas GP, Lewis AW. Maximization of energy capture by a wave-energy point absorber using model predictive control. In: Proc 18th IFAC world congress, 2011. 2011, September, preprint.
[34] Li G, Belmont MR. Model predictive contol of a sea-wave energy converter – part I: a convex approach for the case of a single device. Renew Energy 2014;69:453–63.
[35] Fusco F, Ringwood JV. Short-term wave forecasting for real-time control of wave energy converters. IEEE Trans Sustain Energy 2010;1(2):99–106.
[36] Falnes J. Ocean waves and oscillating systems: linear interactions including wave energy extraction. Cambridge, UK: Cambridge University Press; 2002.
[37] Evans DV. A theory for wave power absorption by oscillating bodies. J Fluid Mech 1976;77(1):1–25.
[38] Evans DV. Power from water waves. Annu Rev Fluid Mech 1981;13:157–87.
[39] Longuet-Higgins MS. Statistical properties of wave groups in a random sea state. Philos Trans R Soc London Ser A 1984;312(1521):219–50.
[40] Belmont MR, Horwood JMK, Thurley RWF, Baker J. Filters for linear sea-wave prediction. Ocean Eng 2006;33(17–18):2332–51.
[41] Dannenberg J, Naaijen P, Hessner K, den Boom H, Reichert K. The on board wave and motion estimator OWME. In: Proc Int Soc Offshore and Polar Engr Conf. 2010.
[42] Frigaard P, Brorsen M. A time-domain method for separating incident and reflected irregular waves. Technical report. Aalborg: Hydraulics and Coastal

Engineering Laboratory, Department of Civil Engineering, Aalborg University; 1993.
[43] Wu G. Direct simulation and deterministic prediction of large-scale nonlinear wave field. In: [Ph.D. thesis]. Cambridge, MA: Massachusetts Institute of Technology; 2004.
[44] Bull DL, Ochs ME, Laird DL, Boren B, Jepsen RA. Technological cost-reduction pathways for point absorber wave energy converters in the marine hydrokinetic environment. Technical report. Sandia National Laboratories; 2013, October. SAND2013-7204.
[45] Quick D. Autonomous wave energy powerbuoy device commences sea trial; 2011, August http://www.gizmag.com
[46] Falnes J. Wave-energy conversion through relative motion between two single-mode oscillating bodies. In: Proc ASME Offshore Mechanics and Arctic Engineering Conference. 1998, July.
[47] Korde UA. Performance of two 2-body heaving axisymmetric wave energy converters under control in irregular waves. In: Proc 11th European wave and tidal energy conference (EWTEC). 2015, September.
[48] Lamb H. Hydrodynamics. 6th ed. UK: Cambridge University Press; 1932. p. 1945 [reissued by Dover, NY].
[49] Whitham GB. Linear and Nonlinear Waves. NY: A Wiley-Interscience Publication, John Wiley & Sons; 1973.
[50] Schetzen M. The Volterra and Wiener theories of nonlinear systems. NY: A Wiley-Interscience Publication, John Wiley & Sons; 1980.
[51] Gradshteyn IS, Ryzhik IM. In: Alan Jeffrey, editor. Table of integrals, series, and products. 5th ed. San Diego, CA: Academic Press; 1994.
[52] Eidsmoen H. On the theory and simulation of heaving-buoy wave-energy converters with control. Trondheim, Norway: Norwegian University of Science and Technology; 1995 [Ph.D. thesis].
[53] Cummins W. The impulse response function and ship motions. Technical report; 1962. p. 101–9. David Taylor Model Basin DTNSRDC.
[54] O'Neill PV. Advanced engineering mathematics. 7th ed. CT: Cengage Learning; 2012.
[55] Korde UA, Ertekin RC. Wave energy conversion by controlled floating and submerged cylindrical buoys. J Ocean Eng Mar Energy 2015;1(3):255–72.